




# Thermal neutron conversion by high purity $^{10}\text{B}$ -enriched layers: PLD-growth, thickness-dependence and neutron-detection performances

Anna Paola Caricato<sup>1,2,a</sup> , Maura Cesaria<sup>1</sup>, Paolo Finocchiaro<sup>4</sup>, Simone Amaducci<sup>4</sup>, Fabio Longhitano<sup>5</sup>, Chiara Provenzano<sup>2,6</sup>, Marcella Marra<sup>1,2</sup>, Maurizio Martino<sup>1,2</sup>, Muhammad Rizwan Aziz<sup>1</sup>, Antonio Serra<sup>1,2</sup>, Daniela Manno<sup>1,2</sup>, Lucio Calcagnile<sup>2,3</sup>, Gianluca Quarta<sup>2,3</sup>

<sup>1</sup> Department of Mathematics and Physics “Ennio De Giorgi”, University of Salento, Lecce, Italy

<sup>2</sup> National Institute of Nuclear Physics (INFN), Lecce, Italy

<sup>3</sup> CEDAD (Centro of Applied Physics, Dating and Diagnostics)-Department of Mathematics and Physics “Ennio De Giorgi”, University of Salento, Lecce, Italy

<sup>4</sup> National Institute of Nuclear Physics (INFN) – Laboratori Nazionali del Sud, Catania, Italy

<sup>5</sup> National Institute of Nuclear Physics (INFN) – Sezione Di Catania, Catania, Italy

<sup>6</sup> Department of Engineering for Innovation, University of Salento, Lecce, Italy

Received: 6 July 2021 / Accepted: 24 February 2022

© The Author(s) 2022

**Abstract** Neutron applications and detection are of paramount importance in industry, medicine, scientific research, homeland security, production of extreme UV optics and so on. Neutron detection requires a converter element that, as a result of its interaction with neutrons, produces reaction products (mainly charged particles) whose detection can be correlated with the neutron flux. Reduced availability and increased cost of the most used converter element,  $^3\text{He}$ , have triggered research efforts for alternative materials, proper deposition methods and new detector architectures.  $^{10}\text{B}$  converter is a valid alternative to  $^3\text{He}$  thanks to its high thermal neutron cross section and relatively high Q value. In this paper we report on the room temperature Pulsed Laser Deposition (PLD) of high quality and uniform  $^{10}\text{B}$  films with the expected density, different thickness values (0.5, 1.0, 1.2, 1.5 and 2.0  $\mu\text{m}$ ) and uniform thickness over a circular area of about 30 mm in diameter. Additionally, they are adherent to the substrate with a negligible presence of contaminants. The conversion properties of such  $^{10}\text{B}$  coatings coupled to a Si solid state detector are studied upon exposure to a neutron flux from an Am-Be neutron source ( $2.2 \cdot 10^6$  n/s). The experimental results, compared with spectra simulated by using a GEANT4 code, present a good agreement and efficiencies of the order of a few percent.

## 1 Introduction

Neutron detection plays an important role in many scientific disciplines, industry and medicine, for several applications, such as radiation portal monitors for home-land security and nuclear safeguards, workplace safety, screening cargo containers, material investigation based on neutron scattering, energy production and neutron monitoring in nuclear power plants, nuclear power instrumentation, cancer therapy and more [1–4].

Since neutrons hold no electric charge, their detection methods generally rely on second-order effects associated with a conversion process whereby an incident neutron interacting with a nucleus produces secondary charged particles. Hence, direct detection of these charged particles by conventional methods (scintillation, gas ionization or solid-state detection) [5] is exploited to reveal the presence of neutrons.

$^3\text{He}$  has been used for long time as the main conversion element in neutron detectors because of its high cross section for thermal neutrons (5330 barn) and high Q energy values released in the reaction [5, 6]. Moreover,  $^3\text{He}$ -based neutron detectors are characterized by high efficiencies and are almost insensitive to radiation other than thermal neutrons [7]. However, over the last years the severe lack and the increasing cost of  $^3\text{He}$  have triggered a worldwide R&D program seeking new technologies, architectures and materials for neutron detection purposes [3, 7–9]. The choice of material, architecture and detector is strictly related to the efficiency requirements and improvements as well as application.

Regarding the conversion element, it can be a component of the detector itself [10–12] or it can be introduced as a separate layer to be coupled with a detector [13–20].

Many newly proposed neutron detection schemes make use of semiconductor detectors for monitoring the production of charged particles (in particular Si-based detectors) instead of gaseous or scintillation detectors. Semiconductor-based neutron detectors are

<sup>a</sup> e-mail: [annapaola.caricato@unisalento.it](mailto:annapaola.caricato@unisalento.it) (corresponding author)

compact, lightweight, less expensive to fabricate, able to operate at low voltage and, importantly, easy to be integrated with the readout electronics.

Recent neutron detection devices are based on boron (B) and B-based compounds as converter elements alternative to  $^3\text{He}$  not only because of their more abundance but also due to their outstanding physical properties. Among these, there are high hardness (comparable to diamond), high stability of B-B bonds, corrosion resistance, low densities, high melting temperatures, high reflectance in the extreme ultraviolet (40 nm—200 nm), as well as tunable thermal and electric transport properties depending on the dimensionality (thin films, nanowires, boron fullerene, borophene) [21–24]. Moreover,  $^{10}\text{B}$  has a very high capture cross section for thermal neutrons (3840 barn) [5, 6].

Depositing pure B films is challenging because of its high melting point and light weight of B. Furthermore, several drawbacks result from a few physical properties of B: (i) the low thermal conductivity and brittle nature cause B targets to disintegrate under thermal loads [25] and, (ii) when B is directly evaporated on the silicon surface of a detector, a deterioration of the surface barrier of the detector was reported [26].

For these reasons, B-based compounds are preferred to pure B in the neutron detection field. Of course, the probability of a neutron capture event in the converter layer and the probability of reaction products to exit from the converter layers are different for pure  $^{10}\text{B}$  with respect to its compounds.

Most papers deal with  $\text{B}_4\text{C}$ , either natural  $\text{B}_4\text{C}$  ( $^{nat}\text{B}_4\text{C}$ ) or enriched  $\text{B}_4\text{C}$  ( $^{en}\text{B}_4\text{C}$ ), since it is less expensive than pure  $^{10}\text{B}$  and can be more easily deposited with standard deposition techniques, like thermal evaporation or sputtering. However, depositing  $\text{B}_4\text{C}$  has some practical problems such as preserving the stoichiometry [20, 27] and poor adhesion to the common substrates could result from hardness-related high intrinsic stress build up during thickening of the growing film ( $\text{B}_4\text{C}$  is the fourth hardest material). This aspect limits the maximum thickness of the film unless soft substrates or heated substrate are used as strategies to reduce/relax the stress [27].

In a recent paper [28], the authors have presented preliminary results on the potentialities of the PLD technique in depositing  $\mu\text{m}$ -thick enriched  $^{10}\text{B}$  films (>95% of enrichment) on Al substrates with a thickness uniformity of 10% over a circular area of 3 cm in diameter.

Going beyond these early findings, in this paper we adopt the optimized deposition conditions discussed in ref [28] and present a more systematic investigation of PLD-grown  $^{10}\text{B}$  films by extending our characterization to morphological, structural, density and compositional aspects as well as by varying the thickness to study thickness-dependent thermal neutron conversion performances when coupled to a Si solid state detector and exposed to a neutron flux.

In particular, accurate film characterization is an important step to properly assess the  $^{10}\text{B}$  conversion behavior and relate it to simulation results and neutron detection performances (being confident of the  $^{10}\text{B}$  film properties, it is possible to critically discuss the correlation between experimental and simulation results excluding some causes of any inconsistencies).

Noteworthy, the choice of thickness as a critical parameter of our study is motivated by its key role in the detector designing step for achieving effective sensing depending on the energy of the charged particles released in the conversion reaction. Indeed, the optimal film thickness can be found by the balance between a large number of neutron reactions associated with thicker films and the lower energy loss of the reaction products, and then increased detection sensitivity, as associated with thinner films. Moreover, thickness-dependent adhesion failure or exfoliation of a B-film can occur due to stress. Hence, the meaning of thicker or thinner thickness has to be carefully calibrated to balance pros and cons related to both design of an efficient neutron detector and avoidance of mechanical failure.

In the outlined context, main goals of this study are: (i) a detailed characterization of  $^{10}\text{B}$  micron thick-films deposited by laser ablation as a fundamental prerequisite to correctly understand the behavior as conversion layer of  $^{10}\text{B}$ ; (ii) study of  $^{10}\text{B}$  thickness-dependent thermal neutron conversion performances both at the experimental level, when coupled to a Si solid state detector exposed to a fixed and calibrated neutron flux from an Am-Be neutron source ( $2.2 \cdot 10^6$  n/s), and at the conceptual level by comparing experimental results and spectra simulated by using a GEANT4 code as a function of thickness.

## 2 Experimental details and characterization methods

### 2.1 PLD depositions

Growth of  $^{10}\text{B}$  layers by PLD has been carried out in a stainless-steel vacuum chamber evacuated down to a base pressure of the order of  $10^{-6}$  Pa by a combined (rotative plus turbomolecular) system of vacuum pumps.

The films under consideration in this study have been deposited by ablating a commercial 95%  $^{10}\text{B}$  enriched high purity (99.9%) B sintered target (American Elements Company, USA) by the fundamental harmonic (*i.e.*, operating wavelength of 1064 nm) of a Q-switched Continuum Powerlite-8010 Nd:YAG laser with pulse width of 7 ns. The laser beam has been focused, by means of a lens, on the enriched  $^{10}\text{B}$  target at an incidence angle of  $45^\circ$  in order to obtain a spot area on the target of about  $4 \text{ mm}^2$  and a laser fluence of  $F \cong 11 \text{ J/cm}^2$ . The laser repetition rate has been fixed at 10 Hz. During laser irradiation, the  $^{10}\text{B}$  bulk target has been kept at room temperature and rotated with an angular speed of 1 Hz and simultaneously spanned, to avoid the formation of craters under multiple irradiations of the same area.

The ablated material has been collected on a suitable substrate, placed in front of the target at 40 mm distance and with axis shifted with respect to the plume axis (shifted-axis configuration). More details about the PLD experimental apparatus and configuration are reported elsewhere [27].

$^{10}\text{B}$  layers have been grown by changing the thickness: 0.5  $\mu\text{m}$ , 1  $\mu\text{m}$ , 1.2  $\mu\text{m}$ , 1.5  $\mu\text{m}$  and 2.0  $\mu\text{m}$  values have been set in our experiments. Under our growth conditions, a deposition rate of 0.13 nm/s has been evaluated, leading to a deposition run lasting about 125 min for depositing a 1  $\mu\text{m}$  thick  $^{10}\text{B}$  film.

Different substrates have been considered for the deposition, depending on the film characterization: (i) Si/SiO<sub>2</sub> substrates for topographical/morphological Atomic Force Microscopy (AFM) and Scanning Electron Microscope (SEM) analyses and structural characterizations (X-Ray Diffraction (XRD) and Raman Infrared Spectroscopy), (ii) graphite disks for compositional and density measurements by Energy Dispersive X-Ray Spectroscopy (EDS) and Rutherford Backscattering Spectrometry (RBS), and (iii) carbon fiber sheets for neutron detection tests.

In particular, the surface morphology properties of the deposited films have been evaluated for  $^{10}\text{B}$  films deposited on Si/SiO<sub>2</sub> substrates in order to avoid any influence of the substrate morphology on the film morphology. In regard to using different substrates depending on the characterization technique, it is worth observing that such an approach does not impact on our conclusions because of the peculiarity of the deposition technique, low substrate temperature and quite large film thickness.

## 2.2 $^{10}\text{B}$ layers: morphological and structural characterizations

The AFM images have been acquired by a Park-70 Instruments operating in non-contact mode at room temperature in air environment. Silicon cantilevers with a tip radius of about 10 nm, a spring constant  $K = 0.1\text{--}100$  N/m and a resonance frequency of about 300 kHz have been used. Also, AFM has been used to quantify roughness: the reported Root-Mean-Square (RMS) roughness values have been calculated over a 20  $\mu\text{m} \times 20 \mu\text{m}$  area. The reported values are an average over five measurements acquired in different representative area of the films. The uncertainty indicates the standard deviation.

The film thickness has been evaluated using a kind of lift-off procedure, depositing along a line on the bare substrate surface some circular drops of silver paint, which have been removed by acetone after the  $^{10}\text{B}$  film deposition, leaving some holes on the sample. The depth of the holes has been measured by AFM.

Raman spectra have been acquired by means of an InVia Renishaw system equipped with a Leica microscope DMLM and a 514 nm Ar<sup>+</sup> Spectra-Physics laser operating at a maximum power of 25 mW. The analysis has been performed on the B films by using a spot size of 2  $\mu\text{m}$ . A large area of about 25 mm<sup>2</sup> has been mapped in order to determine a characteristic Raman spectrum representative for the entire analyzed region.

The deposited films have been also inspected by SEM analysis using a JEOL-JSM-6480LV Microscope equipped for EDS. XRD analysis has been carried out using a Rigaku Miniflex diffractometer, operating in step-scan mode and employing Cu K $\alpha$  radiation at 30 kV and 100 mA. The measurements have been collected from 10 to 60 deg, with a 0.010 deg step-size and a scan speed of 0.25 deg/min.

## 2.3 $^{10}\text{B}$ layers: elemental/compositional and density characterizations

EDS microanalysis equipped with SEM has been performed to study the elemental distribution in terms of the presence of B and eventual critical contaminants such as oxygen (O), carbon (C) and nitrogen (N) in the deposits, while paying attention to the presence of surface features stemming from the ablation mechanism.

EDS analysis has been carried out by operating with an acceleration voltage of the electron beam of 2 keV. The electron beam has been focused on selected points of a SEM image of the sample and the collected X-ray signal has been processed to obtain spectra with peaks associated with the atomic species within the deposits.

In order to obtain information about the atomic density, isotopic and elemental composition of the deposited films, RBS measurements have been carried out. The analyses have been performed at the in vacuum IBA (Ion Beam Analysis Beam Line) installed at the Centre of Applied Physics and Diagnostics (CEDAD, University of Salento) and based on a 3 MV Tandem Accelerator (High Voltage Engineering Europa BV Mod. 4130HC) [29]. A 2 MeV  $^4\text{He}^{2+}$  ion beam has been used as probe, while backscattered particles at an angle of 170° have been detected by using a PIPS (Passivated Implanted Planar Silicon) detector with a solid angle of 3 msr [30]. The number of ions reaching the samples has been calculated from the total deposited charge obtained by integrating the beam current reaching the samples mounted on the electrically isolated vacuum chamber. Spectra have been acquired and pre-processed by using the GENIE software from Canberra. Experimental data have been fitted and quantitative parameters about composition and film density have been obtained by using the SIMNRA package [31]. RBS analyses have been performed on a 400 nm thick film deposited by PLD as described above on carbon fiber.

## 2.4 Neutron detection: experimental setup, measurements and simulation procedure

In order to test the effectiveness of the five neutron converters, they have been characterized by coupling them in turn with a silicon detector. The detector used is an MSX09-300 from Micron Semiconductor, 3  $\times$  3 cm<sup>2</sup> area and 300  $\mu\text{m}$  thickness. This choice was

**Fig. 1** (Top) The setup exploited for the experimental tests with a neutron source, which was also simulated with the GEANT4 Monte Carlo code. The thicknesses are not in scale. (Bottom left) The silicon detector. (Bottom right) The  $^{10}\text{B}$  converter on the carbon fiber substrate installed facing the silicon

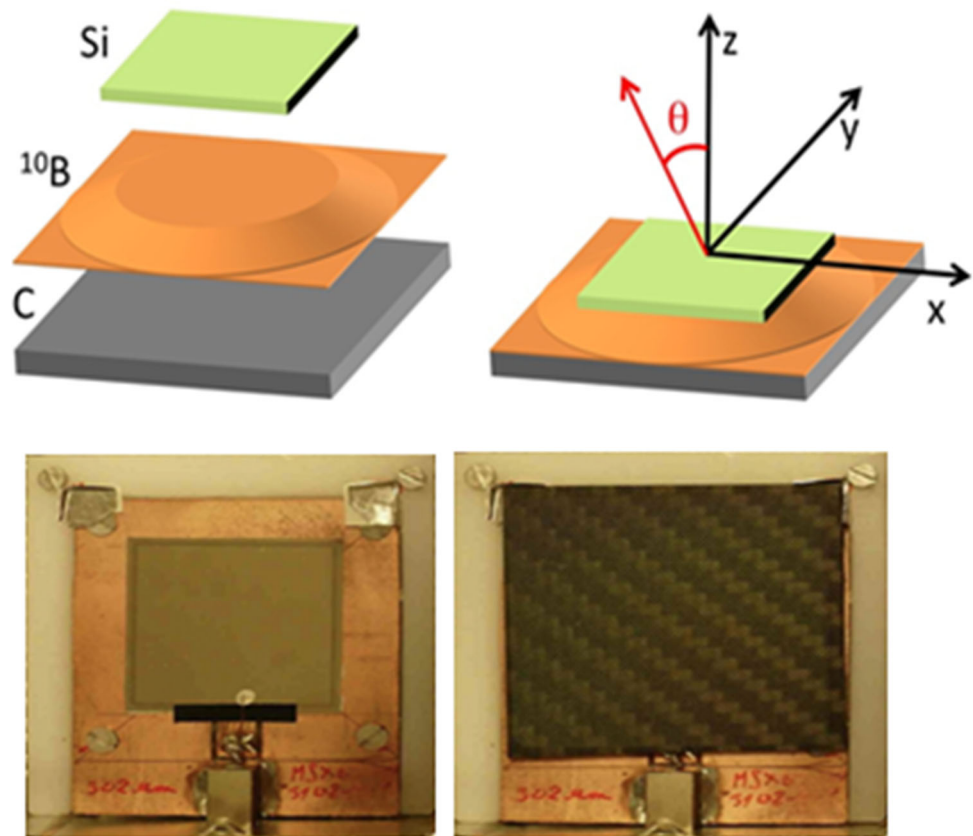
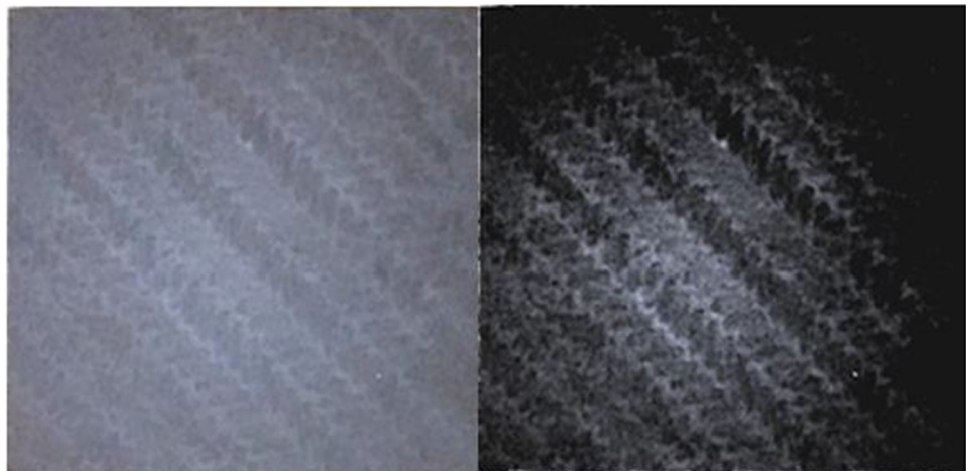


**Fig. 2** (Left) Photograph of the  $0.5\ \mu\text{m}$  sample. (Right) A contrast enhancement makes possible to better appreciate the circular shape of the deposit. In transparency the pattern of the carbon fiber is clearly visible

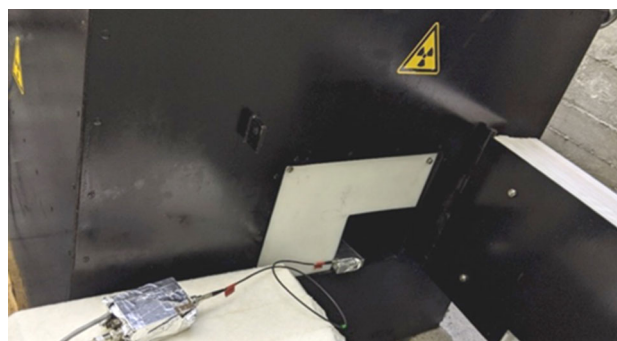


motivated by capacitance and noise related aspects together with costs. The setup, sketched in Fig. 1 top, consists of the  $^{10}\text{B}$  converter deposited onto a  $50 \times 50 \times 1\ \text{mm}^3$  carbon fiber support and placed at  $200\ \mu\text{m}$  from the silicon detector face. The converter shape is a truncated cone, with a 3 cm diameter flat top. The silicon detector has a 300 nm thick aluminized dead layer acting as electric contact. When a neutron interacts with a  $^{10}\text{B}$  nucleus, the produced alpha or  $^7\text{Li}$  particles can reach into the silicon detector after crossing a variable thickness of converter, the thin layer of air and the aluminum dead layer. The silicon detector and the converter facing it are shown in Fig. 1 bottom left-hand side and bottom right-hand side, respectively. The detector was biased at 30 V, the output signal was handled by an ORTEC 142B preamplifier followed by an ORTEC 672 amplifier. The analog-to-digital conversion and the spectra have been obtained by using an Amptek MCA8000A multichannel analyzer.

In the left-hand panel of Fig. 2 we show the photograph of the  $0.5\ \mu\text{m}$  sample, and in the right-hand panel a contrast enhancement makes possible to better appreciate the circular shape of the deposit. In transparency the pattern of the carbon fiber is clearly visible.

The neutron field exploited to test the detection technique with the five boron converters has been produced by an intense AmBe neutron source, available at INFN-LNS, nominally emitting  $2.2 \cdot 10^6$  neutrons/s. The source and its moderator are enclosed in a

**Fig. 3** The measurement position inside the neutron source box. The ORTEC 142B preamplifier is visible on the left, the detector is placed on the edge just inside the source box



$95 \times 75 \times 85 \text{ cm}^3$  iron box. The source is surrounded by a first polyethylene case followed by 30 cm thick paraffin that slows down the high energy neutrons (up to 10 MeV) it emits. The outer 5 cm of the shielding is made from borated paraffin that stops the vast majority of the outgoing thermalized neutrons. The measurements have been done in a position just inside the source box, as shown in Fig. 3, which was chosen as reference position. The thermal neutron flux in the reference position was measured by means of an identical silicon detector featuring a  $1.6 \mu\text{m}$  thick  $^6\text{LiF}$  converter on carbon fiber, whose detection efficiency had been previously calibrated in a certified thermal neutron field [18].

The setup geometry and materials have been incorporated into the well-established Monte Carlo GEANT4 code and the response in a thermal neutron field has been then simulated [32]. For each converter  $10^8$  thermal neutrons (energy = 25.3 meV) have been simulated, uniformly distributed on a  $3 \times 3 \text{ cm}^2$  area and impinging perpendicularly on the back of the carbon fiber substrate along the z direction.

### 3 Results and discussion

#### 3.1 Morphology and elemental composition of the conversion layers

Visual inspection of the PLD-grown  $^{10}\text{B}$  conversion layers indicates they are macroscopically uniform and well adherent to the substrate without delamination and cracking. About the stability of our films, it is worth observing that no peeling off from the substrate has been observed, meaning that the  $^{10}\text{B}$  films are very stable and proper for their usage in a neutron detector device.

In Fig. 4a) a secondary electrons SEM image of a 200 nm thick (as determined by AFM measurements)  $^{10}\text{B}$  film, deposited on Si/SiO<sub>2</sub> is shown. It should be noted that this film is representative of the real film morphology being deposited on a flat substrate and was used to determine the deposition rate (0,13 nm/pulse) in order to define the number of laser pulses to deposit the films with the desired thickness values under consideration in this study. The film surface presents a continuous deposit except for the presence of several micro- and nano-aggregates. The occurrence of micrometric and submicrometric spherical structures can be accounted by the deposition of molten droplets ejected from the target during the ablation process (explosive boiling) at the relatively high fluence set in the experiments. Moreover, owed to the low absorption coefficient of boron ( $1.3 \times 10^6 \text{ m}^{-1}$ ) [33] at the laser wavelength 1064 nm, the formation of fragments, that are observable in the SEM image, originates from a thick layer of heated material where a gradient of temperature is highly probable. Small droplets and nuclei concurring to the background continuous part of the films can also be formed by phase condensation phenomena in the highly saturated (due to high fluence value  $11 \text{ J/cm}^2$ ) plasma plume.

The inset of Fig. 4a shows the related EDS spectrum and the Monte Carlo simulation. Fitting yields boron-to-oxygen ratio B/O = 6.15 and film thickness of 185 nm. This thickness value is in agreement with the experimental one as determined by AFM within the experimental error and simulation model.

The detected low percentage of oxygen must be ascribed to re-sputtering and/or intermixing phenomena of the oxygen from the Si/SiO<sub>2</sub> substrate, caused by the high energy species impinging on the substrate. Moreover, residual oxygen in the background of the ablation chamber or water molecules adsorbed on the inner wall of the chamber can be ruled out. This effect is limited to the particular substrate. As a confirmation, oxygen is absent if the film is deposited on oxygen-free substrates, such as graphite disks (see RBS measurements). Figure 4b shows the Backscattered Secondary Electron (BSE) image of the droplets highlighted in Fig. 4a (white line square). The EDS analysis confirms that these structures are composed almost exclusively of B, as evidenced by the compositional analysis maps reported in Fig. 4c) (boron map) and Fig. 4d) (oxygen map) of the same morphological detail.

The film morphology is confirmed by AFM images (Fig. 5) from which roughness values has been obtained. In particular, an average roughness and an RMS-surface values of  $(53 \pm 8) \text{ nm}$  and of  $(60 \pm 10) \text{ nm}$  have been estimated over a scan area of  $20 \mu\text{m} \times 20 \mu\text{m}$ .

This roughness values are expected to have no impact on the neutron detection efficiency [34].

**Fig. 4** **a** Secondary electrons SEM image of a  $^{10}\text{B}$  film (200 nm) deposited on  $\text{Si}/\text{SiO}_2$  substrate by PLD. The inset shows the related EDS spectrum and the Monte Carlo simulation. **b** BSE image of a droplet with the compositional elemental analysis map on a droplet: **c** boron and **d** oxygen signals

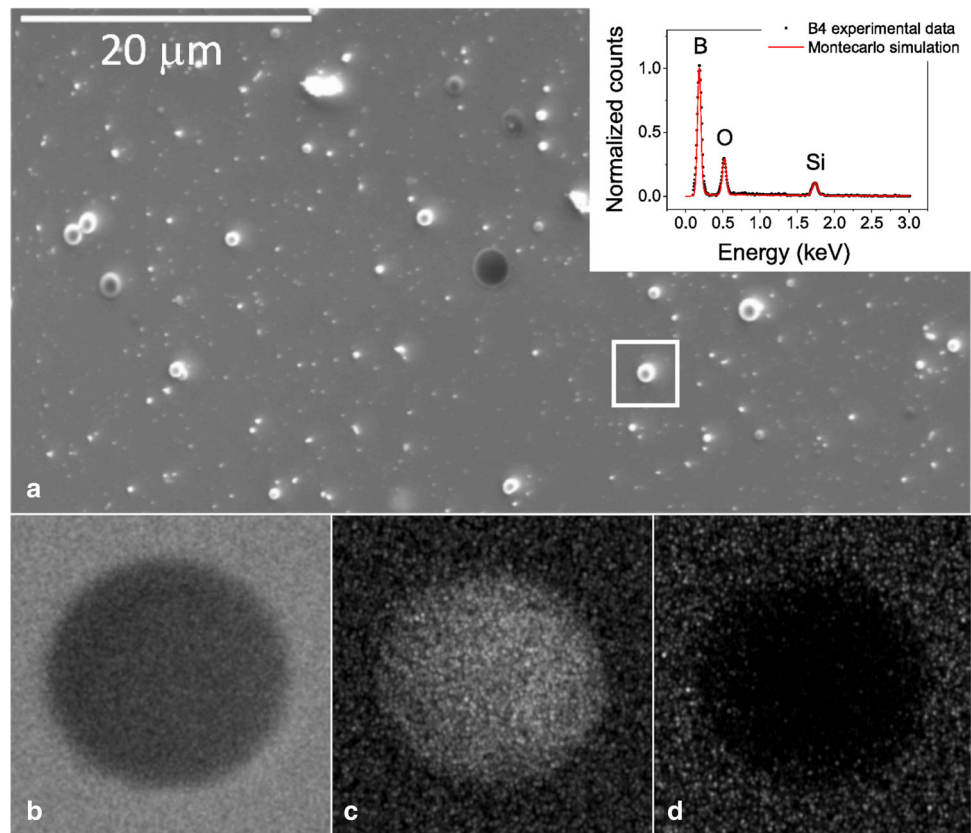
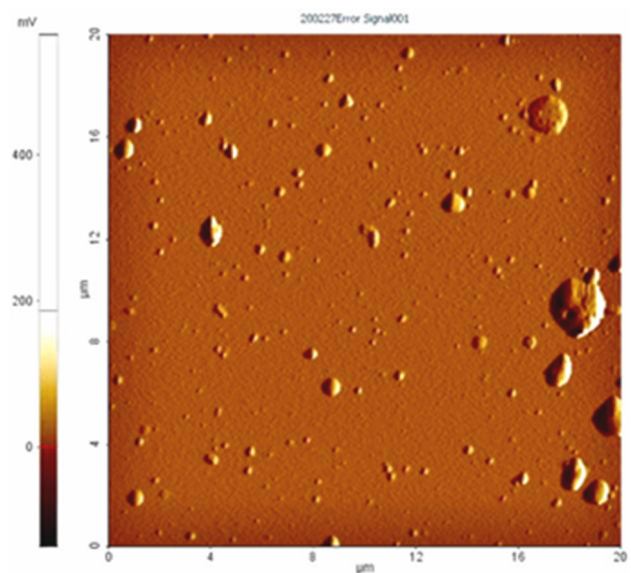


**Fig. 5** AFM image (over a  $20 \times 20 \mu\text{m}^2$  area) of a  $^{10}\text{B}$  film deposited on  $\text{Si}/\text{SiO}_2$  substrate by PLD



### 3.2 Structural and spectroscopic characterization

Microstructure of the  $^{10}\text{B}$  films deposited by PLD on  $\text{Si}/\text{SiO}_2$  substrates has been characterized by XRD and Raman spectroscopy.

The XRD spectrum of the  $^{10}\text{B}$  film, shown in Fig. 6 after the subtraction of the substrate contribution, shows the occurrence of two main broad bands with very different intensities, which are clearly indicative of the presence of an amorphous phase. The measured spectrum can be deconvoluted with three Gaussian curves, peaked around  $2\theta = 21^\circ$ ,  $2\theta = 36^\circ$  and  $2\theta = 43^\circ$ . In Table 1, the peak positions are reported together with the corresponding interplanar distances and reflections. Reflections occurring in the range  $20\text{--}50^\circ$  are typical of amorphous B phase [35, 36] in which some degree of order related to the presence of icosahedral units can be inferred.

**Fig. 6** Typical XRD spectrum of the  $^{10}\text{B}$  films deposited by PLD on  $\text{Si}/\text{SiO}_2$  substrates. The peaks are labeled with the related Miller indices

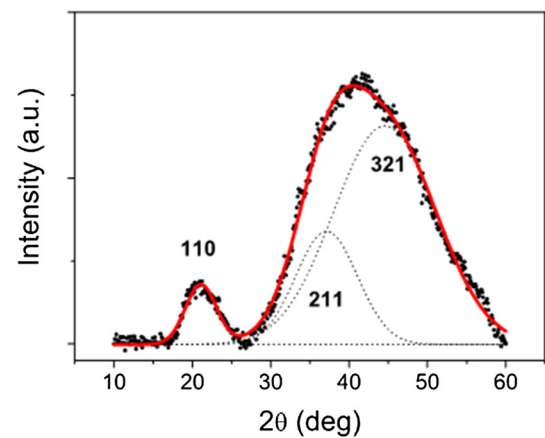
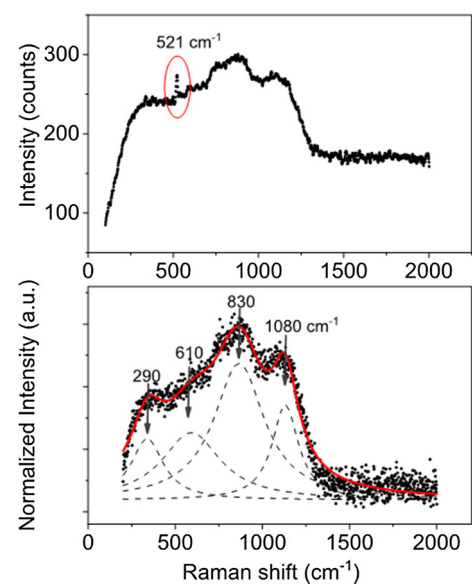


**Table 1** Peak positions, interplanar distances, and reflections of a typical  $^{10}\text{B}$  film deposited by PLD

$2\theta$ (deg)	This work $d$ (nm)	Literature data $d$ (nm)	$hkl$
$20.7 \pm 0.2$	0.43	0.42	110
$37.2 \pm 0.3$	0.25	0.25	211
$44.1 \pm 0.5$	0.17	0.17	321

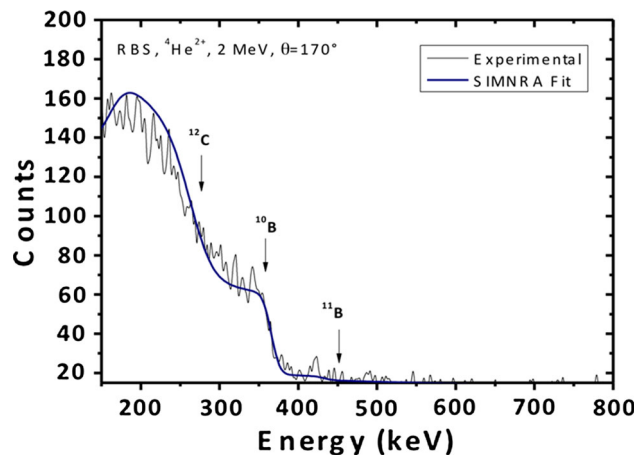
**Fig. 7** (Top) Typical Raman spectrum of the  $^{10}\text{B}$  films deposited by PLD on  $\text{Si}/\text{SiO}_2$  substrates. (Bottom) Deconvolution of the Raman spectrum of the  $^{10}\text{B}$  films deposited by PLD



A deeper knowledge of structure and stoichiometry of the PLD-deposited B-films was gained by Raman analysis of a representative typical  $^{10}\text{B}$  conversion layer deposited on  $\text{Si}/\text{SiO}_2$ . The Raman spectrum (Fig. 7 Top) presents a wide band extending from 200 to  $1200\text{ cm}^{-1}$ , which indicates amorphous nature of the film, and a peak at  $521\text{ cm}^{-1}$  (Fig. 8 Top) due to the silicon substrate [37, 38]. Overall, Raman spectra of boron compounds exhibit two principal spectral regions related to vibrational modes according to the following identification: (i) a spectral range between 400 and  $1100\text{ cm}^{-1}$  associated with intra-icosahedral B-B vibrations; (ii) a low wavenumber region ranging from 200 to  $400\text{ cm}^{-1}$  related to modes involving chains consisting of icosahedra and intermediate atoms (*i.e.*, boron and oxygen atoms or other elements in boron compounds). Among modes classified at the point (ii), incorporation of oxygen from the substrate in the film may cause the formation of B–O covalent/ionic bonds replacing covalent B–B bonds [39].

The measured Raman spectrum processed by subtraction of the substrate contribution and peak deconvolution (Fig. 7 Bottom) enables to identify four defined bands at nearly  $290\text{ cm}^{-1}$ ,  $610\text{ cm}^{-1}$ ,  $830\text{ cm}^{-1}$  and  $1080\text{ cm}^{-1}$ , which are indicative of the occurrence of ordering [40]. The results suggest a not completely amorphous nature of the B-films under consideration in this study. This finding is not surprising, accounting for the accomplished room temperature growth and boron thermal properties. Whereas boron has both crystalline (with multiple allotropes) and amorphous structures [36, 41], amorphous and mixed-phase boron are more commonly found because crystallization of boron occurs at high temperature ( $\sim 1200\text{ }^\circ\text{C}$ ). The high melting temperature of

**Fig. 8** RBS spectrum obtained on a 400 nm PLD film deposited on carbon fiber



boron makes difficult growing boron films by ordinary evaporation [42]. On the other hand, the so-called amorphous boron exhibits a short-range order structure, in which the arrangement of  $\beta$ -icosahedron is close to the  $\beta$ -rhombohedral boron [29].

The preparation of pure and crystallized (amorphous-crystalline mixed grains) boron films by PLD demands growth at very high temperature ( $\sim 800$ – $1000$  °C) and/or gas-phase promoted nucleation [29], the latter mechanism being a more effective process inducing crystallization through the nucleation of crystalline nuclei or clusters of boron in gas-confined ablation plasma plume. In our experiments, as plume expansion occurs in vacuum, condensation in the plasma plume is expected to yield smaller crystallites than in the presence of an inert background gas. As  $\beta$ -rhombohedral boron crystallizes from melt easily and melt cooling results in predominantly amorphous boron [36], it can be supposed that room temperature PLD films may consist of amorphous boron predominantly including  $\beta$ -rhombohedral boron inclusions and/or small crystallites as condensation products.

The RBS spectrum acquired on a 400 nm-thick isotopically enriched  $^{10}\text{B}$  film deposited on carbon fiber is shown in Fig. 8. The signals corresponding to the two boron isotopes are clearly identified as well as the  $^{12}\text{C}$  signal of particles backscattered by the substrate. The best fit of the spectrum was obtained by assuming a thickness of  $5.0 \times 10^{18}$  atoms/cm<sup>2</sup> and an isotopic composition of the target corresponding to what declared by the supplier (American Elements), *i.e.* 96%  $^{10}\text{B}$  and 4%  $^{11}\text{B}$ . By using the measured thickness for the analyzed film (400 nm), this results in a mass density of 2.24 g/cm<sup>3</sup> which is consistent with what expected for a  $^{10}\text{B}$ -enriched boron film and an amorphous boron phase including  $\beta$ -rhombohedral boron inclusions and/or small crystallites confirming the occurrence of a short-range ordering, as resulted from XRD and Raman spectra. Additionally, density as related to the phase of a  $^{10}\text{B}$  film is also important because hardness-related intrinsic stress buildup causes cracking and delamination for progressing growth. Hence, the proper interplay between amorphous  $\beta$ -rhombohedral phase and density as resulting from calibrated PLD experiments can be responsible of the observed mechanical stability.

We also highlight that, within the sensitivity of the technique, the presence of C and O contaminations in the film can be discarded. According to the deposition conditions, these results do not depend on the film thickness but on background pressure and target purity.

## 4 Neutron detection characterizations and performances

### 4.1 Simulation results

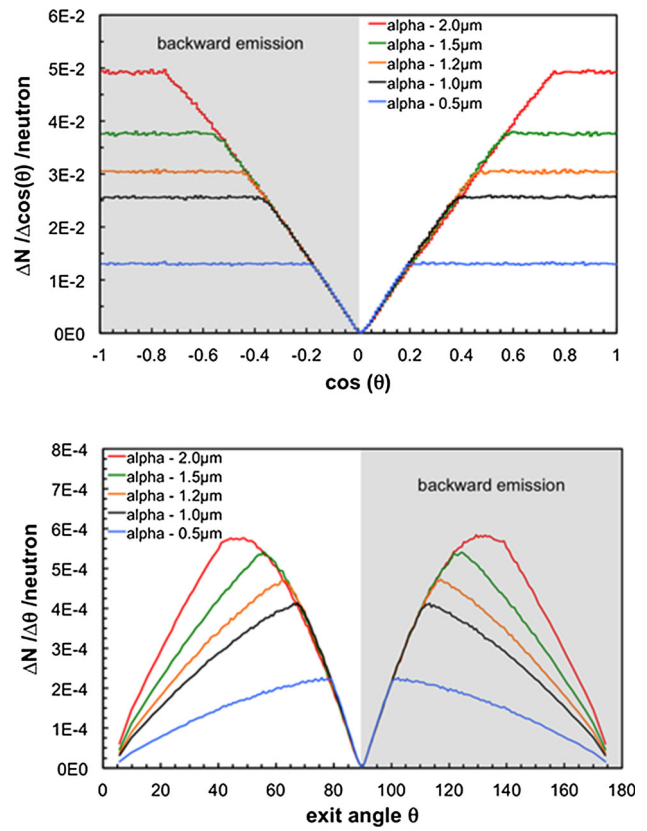
For each neutron interaction all the relevant kinematic parameters have been recorded, so that the properties of the converter could be studied. In Fig. 9 (Top), we show the distribution of the initial z-direction cosine of the alpha particles exiting the five boron samples. If all the alphas could exit the sample, a flat uniform distribution would be expected, that is instead observed only in a limited angular range. This is obvious because, when the particle trajectory is too inclined, the path of the particle in the converter is longer and so the alpha particle loses all of its energy and stops. This effect clearly increases with thicker boron layers.

In other words, the distribution in terms of  $\cos(\theta)$  clearly highlights the horizontal region corresponding to particles produced (isotropically) at any depth which can exit the converter.

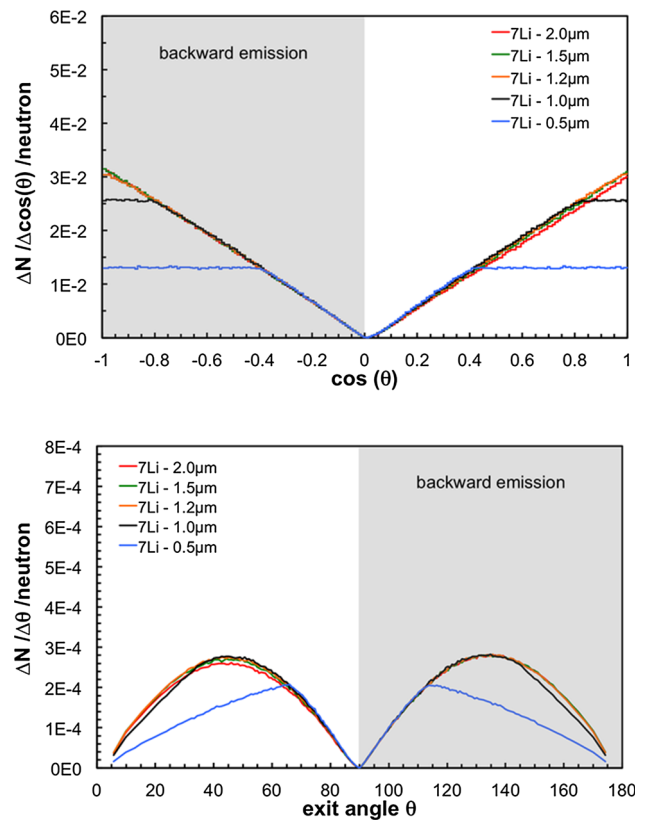
To better describe the situation in terms of an effective geometrical behavior, Fig. 9 (Bottom) shows the same kind of distribution with respect to the exit angle  $\theta$  of the particle. The bump-like shape of the curves is an effect of the solid angle. In Fig. 10, which has the same scales of Fig. 9 on the Y axes, the combined effect of the higher mass and charge and of the lower kinetic energy of the  $^7\text{Li}$  particles is clearly seen. A hint of the flat distribution is only present for the 0.5  $\mu\text{m}$  and the 1.0  $\mu\text{m}$  thicknesses, whereas for the thicker converters there is no angular range where all the particles leave the boron layer.



**Fig. 9** (Top) Distribution of the simulated initial z-direction cosine of the alpha particles exiting the five boron samples. (Bottom) Distribution of the simulated initial angle of the alpha particles exiting the sample



**Fig. 10** (Top) Distribution of the simulated initial z-direction cosine of the <sup>7</sup>Li particles exiting the five boron samples. (Bottom) Distribution of the simulated initial angle of the <sup>7</sup>Li particles exiting the sample



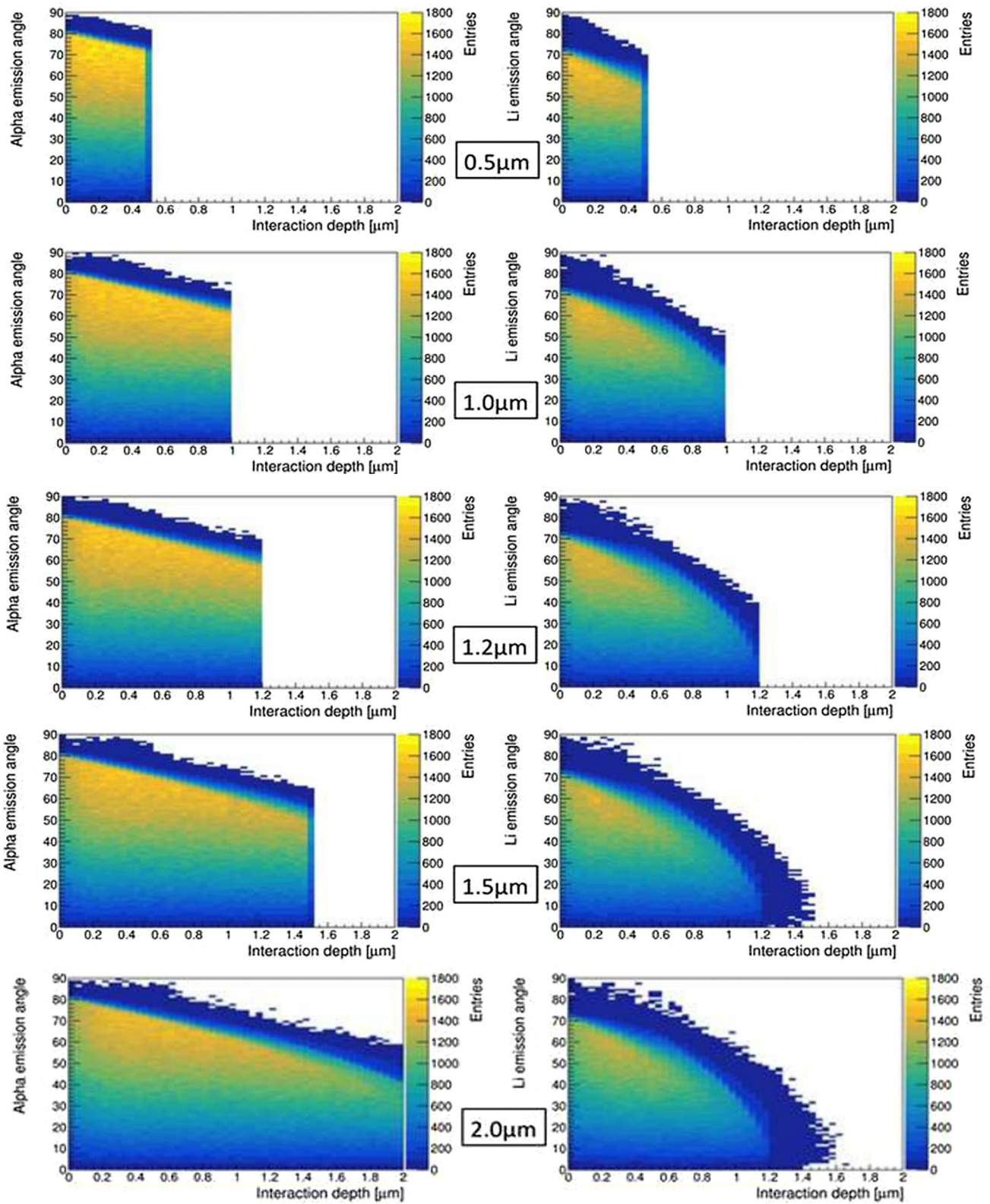


**Fig. 11** Distribution of the number of exiting alphas (left) and  ${}^7\text{Li}$  ions (right) as a function of the interaction depth and of the emission angle, for the 0.5, 1.0, 1.2, 1.5, 2.0  $\mu\text{m}$  thick boron-converter

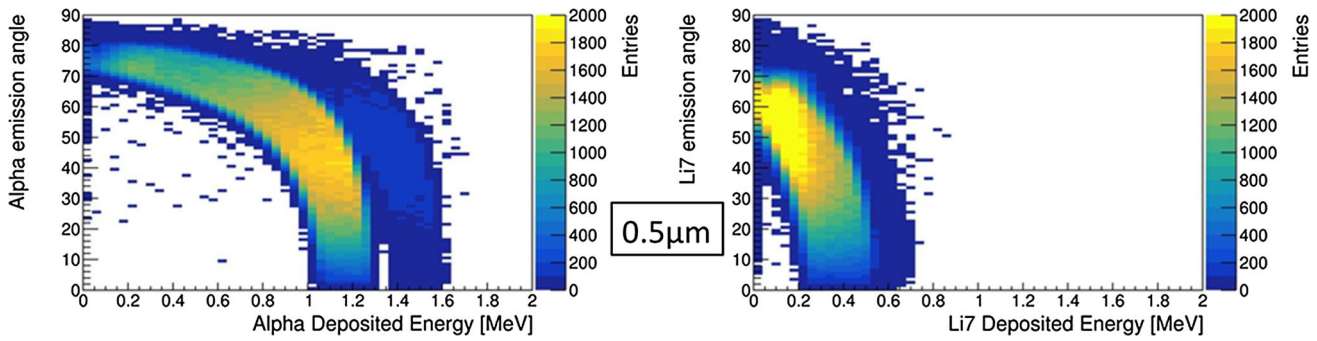


**Fig. 12** Simulation of the number of alphas (left) and <sup>7</sup>Li (right) detected as a function of the deposited energy and of the emission angle for the 0.5 μm thick boron-converter

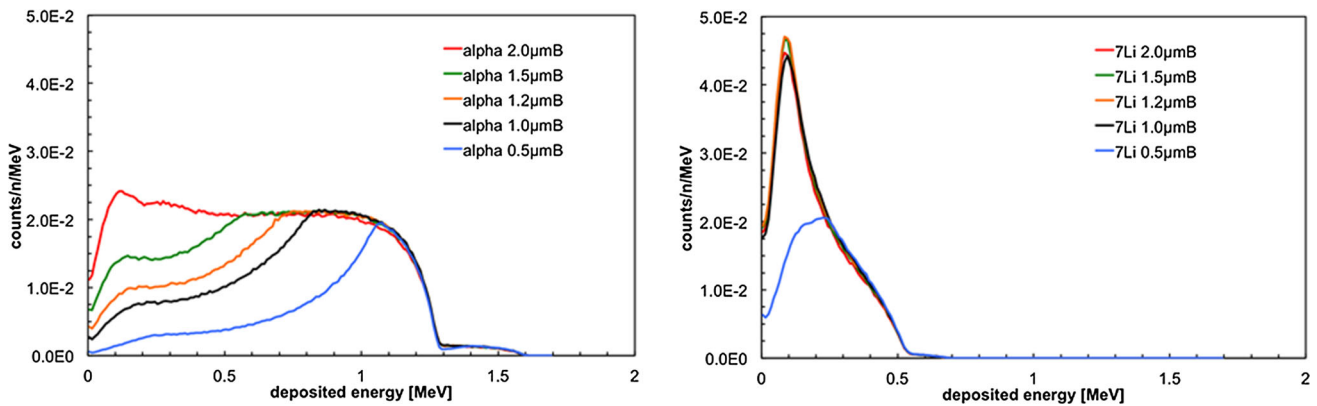
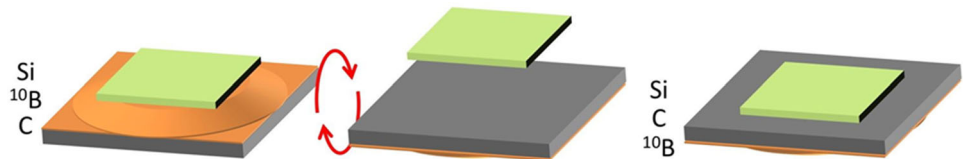


**Fig. 13** Simulation of the deposited energy spectrum of alphas (left) and <sup>7</sup>Li (right) for the five different thicknesses of the PLD-deposited boron-converters

**Fig. 14** The setup exploited for the measurement and subtraction of the gamma ray background: the carbon fiber substrate with the boron layer was turned upside down and placed again in front of the silicon detector



A further insight can be obtained by looking at the 2D scatter plots in Fig. 11, where the distribution of the number of alphas (left) and <sup>7</sup>Li ions (right) leaving the boron layer is reported as a function of both interaction depth and emission angle for the 0.5, 1.0, 1.2, 1.5, 2.0 μm thick boron-converter. It can be seen immediately that, apart from tails with low number of counts, the relevant part of the plot (yellow region) for <sup>7</sup>Li is the same for all the thicknesses ≥ 1.0 μm. This indicates that 1.0 μm is already an upper limiting thickness for <sup>7</sup>Li, and a larger value is counterproductive, as shown in Fig. 10 where the thicker converters give rise to a lower number of counts because the additional thickness acts as a neutron shield. Such an upper limit for alpha particles is visible at 2.0 μm (Fig. 9) and has been determined preliminarily by energy loss code and cross-sectional calculations.

In Fig. 12, we report the 2D scatter plot with the distribution of detected alphas and <sup>7</sup>Li as a function of the emission angle and of the energy deposited into the silicon detector for the 0.5 μm boron converter. By looking at it at constant angle, this plot also highlights the spread of the final detected energy due to the interaction depth inside the converter. The projection of such a plot onto the energy axis is the simulated deposited energy spectrum, which was reported in Fig. 13 for <sup>7</sup>Li and alpha particles for each boron converter thickness. We remark that the blue halo visible in all the plots of Fig. 11 to Fig. 12 is due to the occurrence of the reaction detailed by Eq. 4 along with the dominant one described by Eq. 3.

Due to electronic reasons and to the relevant gamma ray contribution at low energy, a reasonable choice has been made to enforce a threshold at 300 keV, even though the gamma contribution can be subtracted as shown later on. This implies that the <sup>7</sup>Li contribution in the neutron detection by our technique is marginal, as evident in the right panel of Fig. 17. Figure 17 tells us that: (i) the <sup>7</sup>Li contribution basically does not change by increasing the boron thickness upwards from 0.5 μm; (ii) increasing the boron thickness extends the useful contribution of alpha particles toward the lower energy part of the spectrum, and 2 μm basically provides the maximum yield we can obtain. As a consequence, in order to further increase the intrinsic detection efficiency, smarter detection configurations need to be exploited.

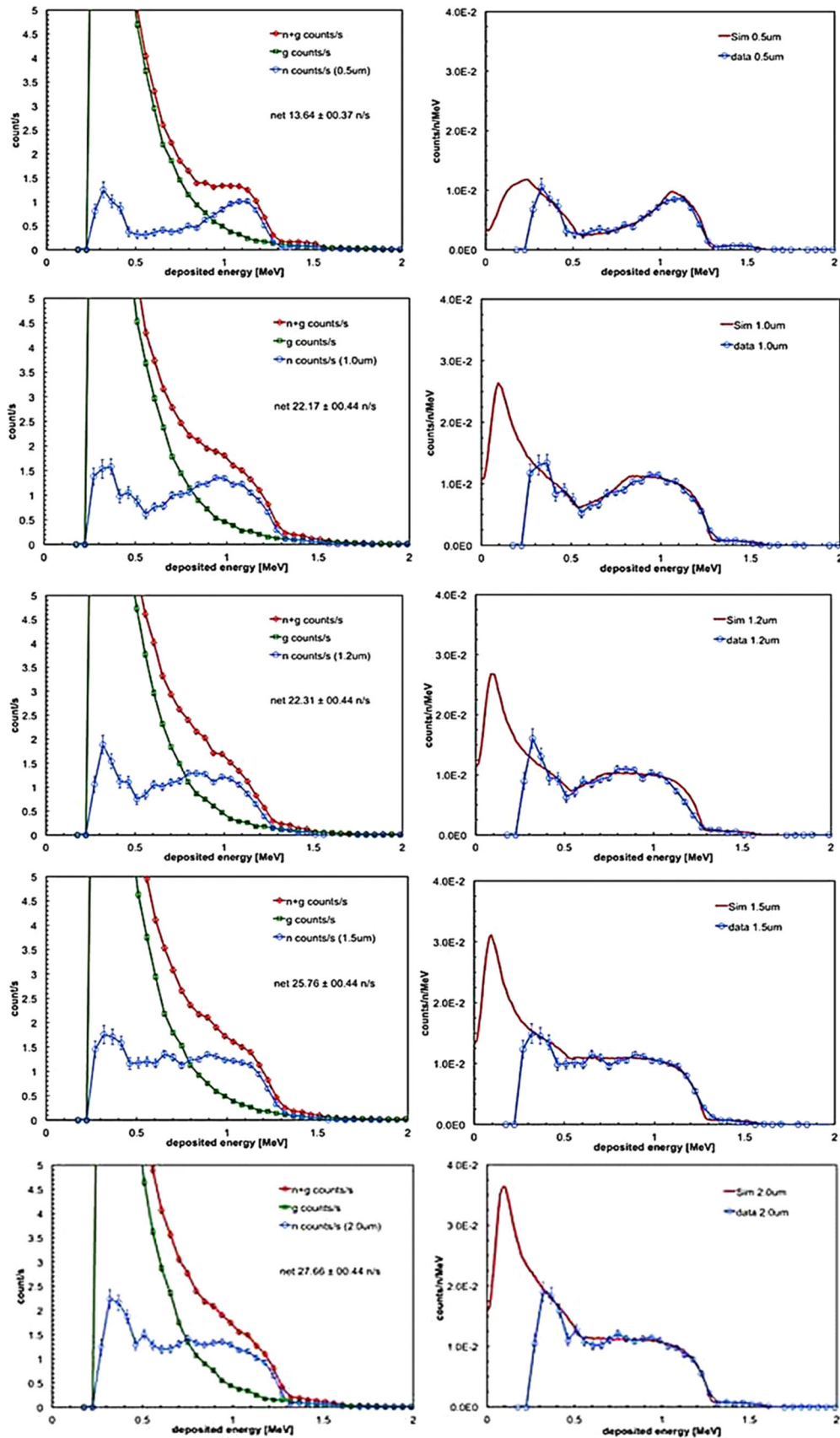


**Fig. 15** Measurements for different thicknesses of the boron converter (0.5, 1.0, 1.2, 1.5, 2.0 μm). (left) Measured counting rate as a function of the deposited energy in the silicon detector and measured background gamma ray contribution; their difference represents the net neutron counts. (right) The net neutron counts compared with the rescaled simulation result (see the text for the explanation of the rescaling)

**Fig. 16** Measured and simulated intrinsic detection efficiency for the PLD-deposited boron converters differing in thickness

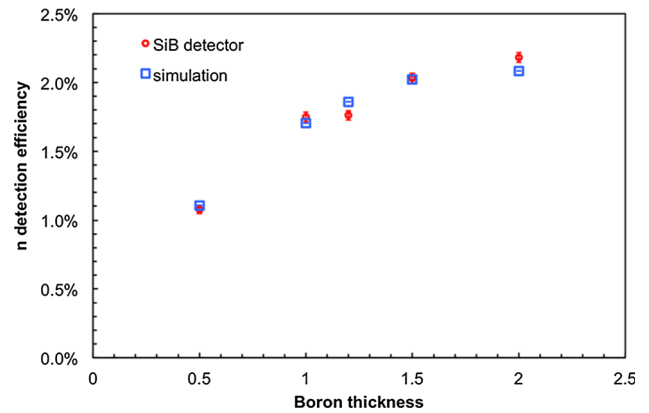
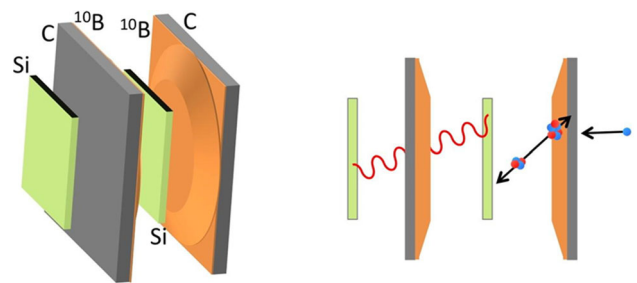


**Fig. 17** Sketch of the proposed configuration for a possible final detector. Only the inner silicon detector sees alpha and  ${}^7\text{Li}$  particles generated in the boron converter. Both silicon detectors see the background gamma radiation whose contribution can then be subtracted



#### 4.2 The measurements of detection efficiency

Turning to the device and its detection efficiency, two measurements have been performed for each boron converter: (i) measurements based on the setup shown in Figs. 1 and 3; (ii) measurements by the setup of Fig. 14, where the converter has been turned upside down in order to measure the contribution of gamma rays. Indeed, the carbon fiber thickness is so large to prevent  ${}^7\text{Li}$  and alphas from reaching the silicon. In the left-hand side plots of Fig. 15, we show the deposited energy spectra which also include the gamma contribution (denoted as  $n + g$ ), the gamma-only spectra (denoted as  $g$ ), and their difference (denoted as  $n$ ) which can be ascribed to the neutron counts for the different boron converter thickness (0.5, 1.0, 1.2, 1.5, 2.0  $\mu\text{m}$ ). As mentioned before, for our evaluations we have taken into consideration the counts starting at 0.3 MeV.

The same measurements have been done by depositing 1.5 micron of  ${}^{10}\text{B}$  on an Al substrate instead of carbon fiber obtaining approximately the same results (not reported here).

In the right-hand side plots of Fig. 15, we show the net neutron counts compared with the rescaled simulation result.

The comparison with the simulations shows a very good agreement in shape but, surprisingly, a rescaling has been needed in order to match the measured and simulated efficiencies.

Being confident of the film properties (which indicate roughness values compatible with good detection efficiency, the absence of contaminants, the right isotopic composition of the converter) as well as of each thickness and density, we ascribe the above discrepancy to the different mechanical structure (giving rise to scattering and hardly adjustable) of our detector with respect to the reference one. By the way, a different density or thickness would clearly influence the spectrum shape, contrary to what has been observed. In future, we plan to assemble a compatible setup in order to directly compare data and simulations.

As a final result, we show in Fig. 16 the measured intrinsic detection efficiency for the five converters, rescaled to compensate for the absorption on the substrate, along with the corresponding simulated values.

## 5 Perspectives

Based on the obtained results we can make several considerations.

Laser ablation has demonstrated to be a powerful technique for the deposition of  ${}^{10}\text{B}$  films. The films are very pure without oxygen contamination and boron oxide formation. The micron-thick films, deposited at room temperature, are very adherent to the substrate and present a good uniformity, of about 10%, over a circular area of 3 cm in diameter.

Respect to  $\text{B}_4\text{C}$  films, B films are responsible for greater efficiency [20]. Due to the smaller number of useful  ${}^{10}\text{B}$  nuclei per unit area, the carbon presence, whose stopping power is higher than boron's, reduces the angular range of the exiting particles. Furthermore it must be considered that the deposition of  $\text{B}_4\text{C}$  generally is such as to produce a non-stoichiometric film (they are generally deficient in B).

It is worth remarking that the above results suggest further discussion and important future perspectives.

We deem that going beyond 2  $\mu\text{m}$  thickness for the converter layer is not convenient, as the intrinsic detection efficiency would tend to saturate and perhaps also start to decrease due to the additional thickness acting as a neutron shield. Therefore, in order to better exploit the features of the  $^{10}\text{B}$  converters, our next step will be to assemble a more efficient setup consisting of a double sandwich of two converters (2  $\mu\text{m}$  thick) and two identical double-sided silicon detectors. The two converters, to be deposited onto boron-free carbon fiber or aluminum, installed on either side of one silicon detector, will double the detection efficiency from  $\approx 2\%$  to  $\approx 4\%$ . The second silicon detector will only see the background gamma radiation and will be used to subtract such a background in order to obtain a net neutron count. This detector configuration is sketched in Fig. 17 and is the subject of an ongoing study.

## 6 Conclusions

In this study, we have extended our recent investigation of deposition and characterization of PLD-grown  $^{10}\text{B}$  films and discussed in detail their performances as neutron detectors, relying on the important and spreading application fields of neutron detectors.

Topographical and morphological analyses have shown that the deposited films are macroscopically uniform without delamination and cracking events affecting their adherence to the substrate. Stability of the films has been observed, which rules out undesirable peeling off from the substrate, deleterious in a neutron detector device. Amorphous-polycrystalline nature of the films is consistent with growth at room temperature. Density, purity, and thickness measurements have been performed to demonstrate the successful PLD-deposition of  $^{10}\text{B}$  layers and careful calibration of the deposition conditions to tune thickness and morphology. Thickness has been demonstrated to be particularly critical in neutron detection designing to efficiently improve the collection efficiency of alpha particles.

Turning to the neutron conversion performances of the PLD-grown B-films, simulations of the dependence of the alpha particle signal on layer thickness and angular spreading have been presented. In this respect, it has been observed that, as increasing the boron thickness extends the useful contribution of alpha particles toward the lower energy part of the spectrum, 2  $\mu\text{m}$  is the thickness yielding the maximum yield. Hence, in practice, improved intrinsic detection efficiency requires different smarter detection configurations.

In addition to neutron detection performances of the single layer, each boron film has been characterized in terms of contribution of gamma rays. The practical negative effects of carbon fiber substrates made with a resin containing boron on attenuating the thermal neutron flux impinging on the converter layers have been addressed to account for unexpected experimental findings.

Moreover, a further device design has been proposed relying on assembling more efficiently the converter layers in a double sandwich of two converters (2  $\mu\text{m}$  thick) and two identical double-sided silicon detectors in order to be able to double the detection efficiency from  $\approx 2\%$  to  $\approx 4\%$  and to subtract the gamma ray contribution.

**Acknowledgements** The research activities leading to this work were supported by the National Institute of Nuclear Physics – INFN (BOLAS and BOLAS\_NEXT projects). A heartfelt acknowledgement is due to Marco Ripani for his constant encouragement and support within the framework of the INFN-E Strategic Project.

**Authors contributions** All authors read and approved the final manuscript. Conceptualization, Methodology, Investigation, Data Curation, Supervision were performed by Paolo Finocchiaro, Anna Paola Caricato and Gianluca Quarta. The first draft of the manuscript was written by Anna Paola Caricato and Paolo Finocchiaro and all authors commented on previous versions of the manuscript. Material preparation, data collection and analysis were performed by Maura Cesaria. PLD depositions and AFM analysis were performed by Chiara Provenzano, Marcella Marra and Muhammad Rizwan Aziz. Raman measurements were performed by Antonio Serra. SEM, EDS and XRD measurements were performed by Daniela Manno. Simulations were performed by Simone Amaducci. Neutron detection tests were performed by Fabio Longhitano. RBS measurements were done by Gianluca Quarta.

**Funding** The work was supported by the Nation Institute of Nuclear Physics (INFN) –BOLAS and BOLAS\_NEXT project

**Data Availability Statement** This manuscript has no associated data or the data will not be deposited. [Authors' comment: There are no associated data available.]

**Code availability** GEANT4.

## Declarations

**Conflict of interest** The authors declare that they have no conflict of interest.

**Ethics approval** The paper and the authors respect ethical policies.

**Consent to participate** All authors agree to participate.

**Consent for publication** All authors agreed with the content and gave explicit consent to submit the paper for publication.

**Open Access** This article is licensed under a Creative Commons Attribution 4.0 International License, which permits use, sharing, adaptation, distribution and reproduction in any medium or format, as long as you give appropriate credit to the original author(s) and the source, provide a link to the Creative Commons licence, and indicate if changes were made. The images or other third party material in this article are included in the article's Creative Commons licence, unless indicated otherwise in a credit line to the material. If material is not included in the article's Creative Commons licence and your intended use is not permitted by statutory regulation or exceeds the permitted use, you will need to obtain permission directly from the copyright holder. To view a copy of this licence, visit <http://creativecommons.org/licenses/by/4.0/>.

## References

- D. Henzlova, R. Kouzes, R. McElroy, P. Peerani, M. Aspinall, K. Baird, A. Bakel, A. Borella, M. Bourne, L. Bourva, F. Cave, R. Chandra, D. Chernikova, S. Croft, G. Dermody, A. Dougan, J. Ely, E. Fanchini, P. Finocchiaro, H. Zhu, Current Status of Helium-3 Alternative Technologies for Nuclear Safeguards, NNSA USDOE and EURATOM, LA-UR-15-21201 (2015).
- A.S. Tremsin, W.B. Feller, R.G. Downing, Efficiency optimization of microchannel plate (MCP) neutron imaging detectors. I. Square channels with 10B doping. Nucl. Instrum. Methods Phys. Res. Sect. A: Accel. Spectrom. Detect. Assoc. Equip. **539**(1), 278–311 (2005)
- K. Zeitelhack, Search for alternative techniques to helium-3 based detectors for neutron scattering applications. Neutron News **23**(4), 10–13 (2012)
- R.T. Kouzes, E.R. Siciliano, J.H. Ely, P.E. Keller, R.J. McConn, Passive neutron detection for interdiction of nuclear material at borders. Nucl. Instrum. Methods Phys. Res. Sect. A **584**(2), 383–400 (2008)
- G. Knoll, *Radiation Detection and Measurement*, 3rd edn. (Wiley, New York, 2000)
- D.A. Brown, M.B. Chadwick, R. Capote, A.C. Kahler, A. Trkov, M.W. Herman, A.A. Sonzogni, Y. Danon, A.D. Carlson, M. Dunn, D.L. Smith, G.M. Hale, G. Arbanas, R. Arcilla, C.R. Bates, B. Beck, B. Becker, F. Brown, R.J. Casperson, J. Conlin, D.E. Cullen, M.A. Descalle, R. Firestone, T. Gaines, K.H. Guber, A.I. Hawari, J. Holmes, T.D. Johnson, T. Kawano, B.C. Kiedrowski, A.J. Koning, S. Kopecky, L. Leal, J.P. Lestone, C. Lubitz, J.I. Márquez Domián, C.M. Mattoon, E.A. McCutchan, S. Mughabghab, P. Navratil, D. Neudecker, G.P.A. Nobre, G. Noguere, M. Paris, M.T. Pigni, A.J. Plompen, B. Pritychenko, V.G. Pronyaev, D. Roubtsov, D. Rochman, P. Romano, P. Schillebeeckx, S. Simakov, M. Sin, I. Sirakov, B. Sleaford, V. Sobes, E.S. Soukhovitskii, I. Stetcu, P. Talou, I. Thompson, S. van der Marck, L. Welsch-Sherrill, D. Wiarda, M. White, J.L. Wormald, R.Q. Wright, M. Zerkle, G. Žerovnik, Y. Zhu, ENDF/B-VIII.0: The 8th major release of the nuclear reaction data library with CIELO-project Cross sections, new standards and thermal scattering data. Nucl. Data Sheets **148**, 1–142 (2018)
- R.T. Kouzes, The 3He Supply Problem, Tech. Rep. PNNL-18388, Pacific Northwest National Laboratory, United States (2009).
- R.T. Kouzes, J.H. Ely, L.E. Erikson, W.J. Kernan, A.T. Lintereur, E.R. Siciliano, D.L. Stephens, D.C. Stromswold, R.M. Van Ginhoven, M.L. Woodring, Neutron detection alternatives to 3He for national security applications. Nucl. Instrum. Methods Phys. Res. Sect. A **623**(3), 1035–1045 (2010)
- R.T. Kouzes, A.T. Lintereur, E.R. Siciliano, Progress in alternative neutron detection to address the helium-3 shortage. Nucl. Instrum. Methods Phys. Res., Sect. A **784**, 172–175 (2015)
- E. Tupitsyn, P. Bhattacharya, E. Rowe, L. Matei, M. Groza, B. Wiggins, A. Burger, A. Stowe, Single crystal of LiInSe<sub>2</sub> semiconductor for neutron detector. Appl. Phys. Lett. **101**(20), 202101 (2012)
- K. Ahmed, R. Dahal, A. Weltz, J.J.Q. Lu, Y. Danon, I.B. Bhat, Solid-state neutron detectors based on thickness scalable hexagonal boron nitride. Appl. Phys. Lett. **110**(2), 023503 (2017)
- J. Blevins, G. Yang, Enabling Ga<sub>2</sub>O<sub>3</sub>'s neutron detection capability with boron doping and conversion layer. J. Appl. Phys. **128**(15), 155706 (2020)
- L. Cosentino, Q. Ducasse, M. Giuffrida, S. Lo Meo, F. Longhitano, C. Marchetta, A. Massara, A. Pappalardo, G. Passaro, S. Russo, P. Finocchiaro, SiLiF Neutron Counters to Monitor Nuclear Materials in the MICADO Project, Sensors **21**(8) (2021).
- D. Reilly, N. Ensslin, H. Smith, Jr., Passive nondestructive assay of nuclear materials, United States, 1991, p. 700.
- D.S. McGregor, M.D. Hammig, Y.H. Yang, H.K. Gersch, R.T. Klann, Design considerations for thin film coated semiconductor thermal neutron detectors—I: basics regarding alpha particle emitting neutron reactive films. Nucl. Instrum. Methods Phys. Res. Sect. A **500**(1), 272–308 (2003)
- M. Barbagallo, L. Cosentino, V. Forcina, C. Marchetta, A. Pappalardo, P. Peerani, C. Scirè, S. Scirè, M. Schillaci, S. Vaccaro, G. Vecchio, P. Finocchiaro, Thermal neutron detection using a silicon pad detector and 6LiF removable converters. Rev. Sci. Instrum. **84**(3), 033503 (2013)
- A. Pappalardo, C. Vasi, P. Finocchiaro, Direct comparison between solid state Silicon+6LiF and 3He gas tube neutron detectors. Results Phys. **6**, 12–13 (2016)
- P. Finocchiaro, L. Cosentino, S. Lo Meo, R. Nolte, D. Radeck, Absolute efficiency calibration of <sup>6</sup>LiF-based solid state thermal neutron detector. Nucl. Instrum. Methods Phys. Res. Sect. A Accel. Spectrom. Detect. Assoc. Equip. **885**, 86–90 (2018)
- D.S. McGregor, J. Kenneth Shultis, Reporting detection efficiency for semiconductor neutron detectors: A need for a standard. Nucl. Instrum. Methods Phys. Res. Sect. A Accel. Spectrom. Detect. Assoc. Equip. **632**(1), 167–174 (2011)
- S. Mehendale, K. Kanaki, M. Povoli, A.T. Samnøy, G. Tambave, A. Kok, C. Höglund, S. Schmidt, S.S. Kazi, I. Llamas-Jansa, T. Kittelmann, C.-C. Lai, T.-E. Hansen, S. Pospíšil, T. Slaviček, D. Röhrich, R. Hall-Wilton, Characterization of boron-coated silicon sensors for thermal neutron detection. Nucl. Instrum. Methods Phys. Res. Sect. A Accel. Spectrom. Detect. Assoc. Equip. **972**, 164124 (2020)
- G.V. Tsagareishvili, F.N. Tavazde, Boron crystals: Preparation, structure and properties. Progress Cryst. Growth Charact. **16**, 341–365 (1988)
- T. Kondo, Recent progress in boron nanomaterials. Sci. Technol. Adv. Mater. **18**(1), 780–804 (2017)
- T.Y. Tian, Z. Guo, T. Zhang, H. Lin, Z. Li, J. Chen, S. Deng, F. Liu, Inorganic boron-based nanostructures: synthesis. Optoelectron. Prop. Prospect. App. Nanomater. **9**, 538 (2019)
- Z. Zhang, E.S. Penev, B.I. Yakobson, Two-dimensional boron: structures, properties and applications. Chem. Soc. Rev. **46**(22), 6746–6763 (2017)
- M. Audronis, P.J. Kelly, A. Leyland, A. Matthews, A New Approach to the Deposition of Elemental Boron and Boron-Based Coatings by Pulsed Magnetron Sputtering of Loosely Packed Boron Powder Targets. Plasma Processes Polym. **4**(S1), S160–S165 (2007)
- A. Rose, Sputtered boron films on silicon surface barrier detectors. Nucl. Inst. Methods **52**(1), 166–170 (1967)
- A.P. Caricato, G. Quarta, D. Manno, M. Cesaria, A. Perrone, M. Martino, A. Serra, L. Calcagnile, G. Barone, A. Lorusso, Wavelength, fluence and substrate-dependent room temperature pulsed laser deposited B-enriched thick films. Appl. Surf. Sci. **483**, 1044–1051 (2019)
- M. Cesaria, A. Lorusso, A.P. Caricato, P. Finocchiaro, S. Amaducci, M. Martino, M.R. Aziz, L. Calcagnile, A. Perrone, G. Quarta, 10B-based films grown by pulsed laser deposition for neutron conversion applications. Appl. Phys. A **126**(6), 404 (2020)
- Z. Wang, Y. Shimizu, T. Sasaki, K. Kirihara, K. Kawaguchi, K. Kimura, N. Koshizaki, Fabrication of crystallized boron films by laser ablation. J. Solid State Chem. **177**(4), 1639–1645 (2004)
- L. Calcagnile, G. Quarta, M. D'Elia, D. Muscogiuri, L. Maruccio, K. Butalag, G. Gianfrate, C. Sanapo, U. Toma, Instrumental developments at the IBA-AMS dating facility at the University of Lecce. Nucl. Instrum. Methods Phys. Res., Sect. B **240**(1), 22–25 (2005)
- M. Meyer, SIMNRA user's guide Report IPP 9/13 Max Planck Institut fur Plasma Physik, Garching (1997) [www.simnra.com](http://www.simnra.com) home.mpcdf.mpg.de/~mam

32. S. Agostinelli, J. Allison, K. Amako, J. Apostolakis, H. Araujo, P. Arce, M. Asai, D. Axen, S. Banerjee, G. Barrand, F. Behner, L. Bellagamba, J. Boudreau, L. Broglia, A. Brunengo, H. Burkhardt, S. Chauvie, J. Chuma, R. Chytráček, G. Cooperman, G. Cosmo, P. Degtyarenko, A. Dell'Acqua, G. Depaola, D. Dietrich, R. Enami, A. Feliciello, C. Ferguson, H. Fesefeldt, G. Folger, F. Foppiano, A. Forti, S. Garelli, S. Giani, R. Giannitrapani, D. Gibin, J.J. Gómez Cadenas, I. González, G. Gracia Abril, G. Greeniaus, W. Greiner, V. Grichine, A. Grossheim, S. Guatelli, P. Gumplinger, R. Hamatsu, K. Hashimoto, H. Hasui, A. Heikkinen, A. Howard, V. Ivanchenko, A. Johnson, F.W. Jones, J. Kallenbach, N. Kanaya, M. Kawabata, Y. Kawabata, M. Kawaguti, S. Kelner, P. Kent, A. Kimura, T. Kodama, R. Kokoulin, M. Kossov, H. Kurashige, E. Lamanna, T. Lampén, V. Lara, V. Lefebvre, F. Lei, M. Liendl, W. Lockman, F. Longo, S. Magni, M. Maire, E. Medernach, K. Minamimoto, P. Mora de Freitas, Y. Morita, K. Murakami, M. Nagamatu, R. Nartallo, P. Nieminen, T. Nishimura, K. Ohtsubo, M. Okamura, S. O'Neale, Y. Oohata, K. Paech, J. Perl, A. Pfeiffer, M.G. Pia, F. Ranjard, A. Rybin, S. Sadilov, E. Di Salvo, G. Santin, T. Sasaki, N. Savvas, Y. Sawada, S. Scherer, S. Sei, V. Sirotenko, D. Smith, N. Starkov, H. Stoecker, J. Sulkimo, M. Takahata, S. Tanaka, E. Tcherniaev, E. Safai Tehrani, M. Tropeano, P. Truscott, H. Uno, L. Urban, P. Urban, M. Verderi, A. Walkden, W. Wander, H. Weber, J.P. Wellisch, T. Wenaus, D.C. Williams, D. Wright, T. Yamada, H. Yoshida, D. Zschesche, Geant4—a simulation toolkit. *Nucl. Instrum. Methods Phys. Res. Sect. A Accel. Spectrom. Detect. Assoc. Equip.* **506**(3), 250–303 (2003)
33. N. Morita, A. Yamamoto, Optical and Electrical Properties of Boron. *Jpn. J. Appl. Phys.* **14**(6), 825–832 (1975)
34. Z. Fang, Y. Yang, Y. Li, X. Wang, The Research on the Effect of Boron Layer Roughness for the Detection Efficiency of Boronlined Gaseous Neutron Detector, 2017 IEEE Nuclear Science Symposium and Medical Imaging Conference (NSS/MIC), 2017, pp. 1–3.
35. E.A. Ekimov, R.A. Sadykov, E.L. Gromnitskaya, M.V. Kondrin, N.N. Mel'nik, Physical and mechanical properties of dense materials produced by hot isostatic pressing of amorphous boron. *Inorg. Mater.* **42**(5), 479–483 (2006)
36. M. Kobayashi, Structure of amorphous boron. *J. Mater. Sci.* **23**(12), 4392–4398 (1988)
37. K. Shirai, Elastic properties and the mechanical stability of icosahedral boron crystals. *Phys. Rev. B* **55**(18), 12235–12243 (1997)
38. Z. Wang, Y. Zhao, P. Lazor, H. Annersten, S.K. Saxena, In situ pressure Raman spectroscopy and mechanical stability of superhard boron suboxide. *Appl. Phys. Lett.* **86**(4), 041911 (2005)
39. D. Music, U. Kreissig, V. Chirita, J.M. Schneider, U. Helmersson, Elastic modulus of amorphous boron suboxide thin films studied by theoretical and experimental methods. *J. Appl. Phys.* **93**(2), 940–944 (2002)
40. D. Dellasega, V. Russo, A. Pezzoli, C. Conti, N. Lecis, E. Besozzi, M. Beghi, C.E. Bottani, M. Passoni, Boron films produced by high energy Pulsed Laser Deposition. *Mater. Des.* **134**, 35–43 (2017)
41. K. Shirai, Phase diagram of boron crystals. *Jpn. J. Appl. Phys.* **56**(5S3), 05FA06 (2017)
42. C.C. Klepper, R.C. Hazelton, E.J. Yadlowsky, E.P. Carlson, M.D. Keitz, J.M. Williams, R.A. Zuhr, D.B. Poker, Amorphous boron coatings produced with vacuum arc deposition technology. *J. Vac. Sci. Technol., A* **20**(3), 725–732 (2002)